Mesostructure and physical properties of aqueous mixtures of the ionic liquid 1-ethyl-3-methyl imidazolium octyl sulfate doped with divalent sulfate salts in the liquid and the mesomorphic states

Oscar Cabeza,*[a] Luisa Segade,[a] Montserrat Domínguez-Pérez,[a] Esther Rilo,[a] David Ausín,[a] Anna Martinelli,[b] Negin Yaghini,[b] Bernhard Gollas,[c] Manfred Kriechbaum,[d] Olga Russina,[e] Alessandro Triolo,[f] Elena López-Lago,[g] and Luis M. Varela[g]

This paper extends the study of the induced temperature change in the mesostructure and in the physical properties occurring in aqueous mixtures of the ionic liquid 1-ethyl-3-methyl imidazolium octyl-sulfate [EMIm][OSO_4]. For some compositions these mixtures undergo a phase transition between the liquid (isotropic in the mesoscale) and the mesomorphic state (lyotropic liquid crystalline) at about room temperature. The behavior of mixtures doped with a divalent metal sulfate in order to observe their applicability as electrolytes. Calcium sulfate salt is almost insoluble even in the 20 $_{wt}$% water mixture. The magnesium salt, in contrast, can be dissolved up to concentrations of 730 ppm in the same mixture and it has a profound impact on its properties. Six aqueous mixtures (with water content from 10 $_{wt}$% to 33 $_{wt}$%) of [EMIm][OSO_4] were saturated with magnesium sulfate salt, producing the ternary mixture [EMIm][OSO_4]+H_2O+$MgSO_4$. Viscosity, density and ionic conductivity for these samples were measured from 10°C to 90°C. In addition, SAXS, FTIR, diffussion NMR and Raman spectroscopy of the most interesting samples have been performed, and structural data indicate a transition between a hexagonal lyotropic liquid crystalline phase below and an isotropic solution phase above room temperature. The octyl sulfate anions of the cylindrical micelles in the hexagonal phase are coordinated with water molecules through H-bonds (about four per sulfate anion), while the [EMIm] cations seem to be poorly coordinated and so free to move. Inorganic salt addition reinforces that network, increasing the phase transition temperature.

How to cite:
O. Cabeza, L. Segade, M. Domínguez-Pérez, E. Rilo, D. Ausín, A. Martinelli, N. Yaghini, B. Gollas, M. Kriechbaum, O. Russina, A. Triolo, E. López-Lago and L. M. Varela, Mesostructure and physical properties of aqueous mixtures of the ionic liquid 1-ethyl-3-methyl imidazolium octyl sulfate doped with divalent sulfate salts in the liquid and the mesomorphic states, *Phys. Chem. Chem. Phys.*, 2018, **20**, 8724–8736.
DOI: 10.1039/C7CP07999K

1. Introduction

Room temperature ionic liquids (ILs) have a combination of physico-chemical properties that make them attractive for many technical applications.[1] Due to their intrinsic ionic conductivity, they have been suggested as non-aqueous electrolytes for electrochemical applications, as the electroplating of base metals and semiconductors and also for energy storage and conversion in e.g. fuel cells, batteries, electrolytic capacitors and dye-sensitized solar cells.[2,3] In all of these applications the electrolyte conductivity and the width of its electrochemical window is a crucial parameter. Compared to usual electrolytes however, the ionic conductivity of most ILs is relatively poor (< 0.1 $S \cdot m^{-1}$). This has recently triggered studies of aqueous mixtures of ILs with the aim of achieving a combination of good bulk ionic conductivity as in aqueous electrolyte solutions, while retaining the beneficial interfacial properties of ILs.[4,5] Attempts have been made to further increase the applicability of such mixtures by adding metal salts, whose impact has been studied both theoretically and experimentally.[6,7]

Alkali salts of long chain alkyl sulfates, e.g. sodium dodecyl sulfate, are anionic surfactants and are known to form micellar aggregates in aqueous solutions. While sodium octyl sulfate is solid up to its decomposition temperature of 195 °C, 1-ethyl-3-methyl imidazolium octyl sulfate [EMIm][OSO_4] is a room temperature ionic liquid, with a solidification temperature of −9 °C.[8,9] This IL is hygroscopic, and viscosity measurements together with polarized light microscopy have indicated the formation of a lyotropic liquid crystalline phase upon mixing with water at temperatures up to 25ºC, depending on the concentration of water, which can be naturally absorbed from the atmospheric moisture.[9]

Such lyotropic mesophases are otherwise formed by adding amphiphiles to a solvent. These form aggregates above the critical micelle concentration, which can have various shapes

[a] *Grupo Mesturas, Universidade da Coruña. Departamento de Física e Ciencias da Terra, Facultade de Ciencias, Campus da Zapateira, 15071 A Coruña, Spain*
[b] *Department of Chemistry and Chemical Engineering. Chalmers University of Technology. Kemigården 4, 41296 Göteborg, Sweden*
[c] *Institute for Chemistry and Technology of Materials. Graz University of Technology. Stremayrgasse 9, 8010 Graz, Austria*
[d] *Institute of Inorganic Chemistry, Graz University of Technology, Stremayrgasse 9, 8010 Graz, Austria*
[e] *Department of Chemistry, Sapienza University, Rome, Italy*
[f] *Laboratorio Liquidi Ionici, Istituto Struttura della Materia, Consiglio Nazionale delle Ricerche (ISM-CNR). Rome, Italy*
[g] *Grupo de Nanomateriales, Fotónica y Materia Blanda. Departamento de Física de Partículas y Departamento de Física Aplicada. Universidade de Santiago de Compostela. Campus Vida, 15782. Santiago de Compostela, Spain.*
*Corresponding author. Tel.: +34981167000 (O. Cabeza). E-mail address: oscar.cabeza@udc.es
Electronic Supplementary Information (ESI) available: [details of any supplementary information available should be included here]. See DOI: 10.1039/C7CP07999K

and sizes and constitute the building blocks of liquid crystals. Usually, the normal topology (or Type 1) phase structures forming upon increasing the amphiphilic concentration range from micellar cubic, *via* hexagonal and bicontinuous cubic, to lamellar.[10] Sometimes a gel phase is observed in between the hexagonal and the lamellar mesophase. A further increase in amphiphilic concentration leads to the formation of inverse topology lyotropic (or Type 2) phases, where the polar domain is discontinuous.

The mesophase structure and behaviour of binary mixtures of ILs and water has attracted considerable interest.[11-14] For dry 1-decyl-3-methyl imidazolium bromide only a single broad Bragg peak is observed in small angle X-ray scattering (SAXS), indicating significant lattice and orientational disorder.[14] Addition of water to the sample to yield a composition containing ≈ 5-40 $_{wt}$% of H_2O results in a strong, anisotropic 2D pattern featuring two diffraction rings, which indicate the presence of a lamellar lyotropic liquid crystalline phase.[14] A characteristic optical texture of the birefringent sample in polarized light microscopy supports this finding. Inoue *et al.* have studied the binary mixture of 1-dodecyl-3-methyl imidazolium bromide and water by differential scanning calorimetry and polarized optical microscopy and found the hexagonal and the lamellar liquid crystalline phase.[12] A similar behaviour observed by SAXS has been reported for 1-hexadecyl-3-methyl imidazolium chloride.[15] Russina *et al.* have studied the water-free IL [EMIm][OSO_4] by SAXS.[16,17] The low-*Q* peak in the SAXS pattern of this and a range of similar ILs, provides evidence for an intermediate range order existing in [EMIm][OSO_4], and other ILs[14,18] with a large variety in the nature and spatial extent of the interactions of heads and tails. As mentioned, the aqueous mixtures of [EMIm][OSO_4] are in a semi-solid liquid crystalline state around room temperature for certain water concentrations (which can be directly absorbed from the atmospheric moisture).[9] These last samples decrease their solidification temperature down to −90 °C.

The application of ILs as electrolytes is promising, but the usage of conducting liquid crystalline phases in a semi solid state and based on ILs is even a more interesting option, and many attempts have been made to have the optimum recipe.[19-24] Common approaches include mixing monomers with an IL and polymerize the mixture,[19-21] adding a gelator to an aqueous mixture of a given IL[22,23] or preparing poly-ILs which self-polymerize.[24] The main problem for the majority of the polymer gel electrolytes based on ILs is that their ionic conductivities drop by about two orders of magnitude with respect to its value in the liquid phase.[24] In the lyotropic liquid crystalline phase that we have discovered, that problem does not appear because the electrical conductivity remains high (> 1 S/m, due to the water presence) through the phase transition.[9]

The addition of active metal salts to ILs results in a redox element that can interchange charge with the electrodes. We have studied [EMIm][OSO_4] + H_2O mixtures doped with univalent salts in a very recent paper,[25] where we proposed a model to explain the mesophase formation, whose transition temperature is affected by the salt nature. Here, we report the phase transition involving the mesostructures experienced by those aqueous mixtures when doped with magnesium or calcium sulfate salts. These are promising cations for electrolytes due to their double charge and, in the case of Mg^{2+}, a similar size to the lithium cation.[22] In addition, Mg and Ca are much more abundant than Li, widely spread on earth and, accordingly, cheaper. More specifically, we present new results based on the use of infrared (IR) and Raman spectroscopy, diffusion nuclear magnetic resonance spectroscopy, SAXS and optical microscopy, which help elucidating the mesostructured of the investigated samples. In addition, experimental values of other relevant properties such as ionic conductivity, density and viscosity as a function of temperature are also provided.

2. Experimental

2.1. Chemicals

The chemicals used are summarized in Table 1, where we include the supplier, purity, water content and molar mass. The water employed to prepare the mixtures was of Milly-Q grade. The IL used here can be also denoted in literature as C_2C_1Im-C_8SO_4. Note that both sulfate salts used are not soluble in the pure IL, being the concentration of the metal in the saturated solution at room temperature about 2 ppm.

2.2. Samples

To begin, we have prepared five different aqueous mixtures of [EMIm][OSO_4] with water content below 33 $_{wt}$%, which is the limit for the formation of a liquid crystal.[9,25] These binary samples were named as (n), and their composition is given in Table 2. This table includes also a pure IL sample, named (0). Part of the volume of each of the aqueous mixtures was saturated with the $MgSO_4$ and, another part, with $CaSO_4$ salt. For that we add excess of the inorganic salt to each binary mixture, airtight sealed the tube and shake well the sample. Then, it is heated up 80 °C for some minutes, ultra-sounded and left at 25 °C for 24 hours to equilibrate the solution. Finally, the clear solution is extracted leaving the salt deposit in the bottom of the tube used. The solubility of the $CaSO_4$ is negligible, thus for example, sample (3) saturated with this salt has about 15 ppm of Ca. In contrast, the same mixture saturated with $MgSO_4$ presents about 60 times higher concentration for the Mg.

Table 1. Supplier, purity, water content and molar mass for the chemicals used

	Supplier	Purity	Water content	Molar mass (g)
[EMIm][OSO_4]	Aldrich	> 98%	560 ppm	320.45
$MgSO_4$	Panreac	> 99%	Anhydrous	120.37
$CaSO_4$	Alfa Aesar	> 99%	Dihydrated	136.14

Table 2. Properties (density, ρ; viscosity, η; and ionic conductivity, κ) experimentally measured; weight percentage composition of the samples; Mg cation content in ppm; molar fraction of the IL, and phase transition temperature of the mesomorphic state for each mixture studied.

Mixture	Mag.	$_{wt}$% IL	$_{wt}$% water	$_{wt}$% Mg Salt	Mg (μg/g)	x_{IL}	T_{RG} (°C)
(0)	ρ, η, κ	99.94	0.06	0.00	< 2	0.989	-
(1)	ρ, η, κ	90.82	9.18	0.00	< 2	0.357	4.5
(2)	ρ, η, κ	83.20	16.80	0.00	< 2	0.218	19.0
(3)	ρ, η, κ	77.42	22.58	0.00	< 2	0.161	17.0
(4)	ρ, η, κ	71.24	28.74	0.00	< 2	0.122	2.0
(5)	κ	66.89	33.11	0.00	< 2	0.102	-
(1+)	κ	90.68	9.16	0.16	310±20	0.357	6.0
(2+)	κ	83.07	16.78	0.15	306±5	0.217	27.0
(3+)	ρ, η, κ	77.05	22.47	0.48	975±7	0.161	27.0
(4+)	κ	70.78	28.58	0.64	1300±20	0.122	12.0
(5+)	κ	65.94	32.94	1.42	2860±50	0.100	1.0
(2.5)	ρ, η, κ	80.63	19.37	0.00	< 2	0.190	20.0
($2.5^1/_3$)	ρ, η, κ	80.53	19.35	0.12	248±2	0.189	20.5
($2.5^2/_3$)	ρ, η, κ	80.44	19.32	0.24	488±2	0.189	26.0
($2.5^3/_4$)	κ	80.42	19.31	0.27	547±2	0.189	28.0
(2.5+)	ρ, η, κ	80.34	19.30	0.36	733±2	0.189	29.0

$u_r(_{wt}\%) = 0.01$ %; $u(x_{IL}) = 0.001$; $u(T_{RG}) = 0.5$ °C

Due to that, the data obtained for the $CaSO_4$ doped samples equal those of the corresponding non-doped liquids within the experimental errors. Therefore, these mixtures were not analysed further.

The samples (n) saturated with the $MgSO_4$ salt have been denoted as (n+), and their compositions are included in Table 2. Finally, a sixth aqueous mixture was prepared with water content between those of (2) and (3) samples, looking for the maximum phase transition temperature, which was named (2.5) and its composition is also included in Table 2. Again, part of this sample was saturated with the Mg sulfate salt as explained above, and it was named sample (2.5+). These last two samples were mixed in different proportions to investigate influence of the salt content on the different measured properties. The composition of these not saturated samples, named as ($2.5^a/_b$), also appears in the bottom lines of Table 2. The fraction $^a/_b$ indicates roughly the (2.5+) mixture weight with respect to the total of the sample. j

2.3. Equipment

All the mixtures were prepared by weight using a Gram ST-510 balance, which has a repeatability of $1{\cdot}10^{-6}$ kg. Moreover, the metal concentration in each sample were measured with a quadrupolar Inductively Coupled Plasma Mass Spectrometry (ICP-MS) Thermo-X with High-Performance Liquid Chromatography (HPLC) in the Research Support Facilities (SAI) of the Universidade da Coruña. Lastly, as far as the determination of the concentration of the samples is concerned, the quantity of water in any of the studied mixtures was obtained by Karl Fisher titration.

Ionic conductivity (κ) was measured using a CRISON GLP31 conductivity meter, which uses a constant ac current of 500 Hz and 4.5 V peak to peak. All measurements were performed in the isothermal basis described below. The experimental uncertainty is less than 0.5 % of the measured value, while the repeatability is better than 3 %. The sample was immersed into a Julabo F25 thermostatic bath which controlled the temperature within 0.1 °C. Ionic conductivity measurements were repeated at least three times at 25 °C. Calibration was performed with two certified KCl solutions every 30 days.

Density and dynamic viscosity (ρ and η, respectively) were simultaneously measured with an Anton Paar Stabinger SVM 3000 viscodensimeter with a repeatability better than $5{\cdot}10^{-4}$ $g{\cdot}cm^{-3}$ and 0.4 % of the measured value, respectively. This device has an internal Peltier thermostat featuring an uncertainty in the temperature of ±0.02 °C from 20 °C to 90 °C. It allows the measurement of viscosities from 0.2 to 20,000 mPa·s without changing any instrumental part, and so it is the most adequate apparatus to measure the phase transition process, where differences of some orders of magnitude in a narrow transition temperature interval from liquid to mesomorphic states appear. In that temperature range the sample is in an intermediate liquid crystalline phase (named quasi-gel state in Ref. 25) as we will see below. All measurements were performed in an isothermal basis, thus the sample is tempered at least 15 minutes at each temperature before measuring it (and more than 30 minutes around phase

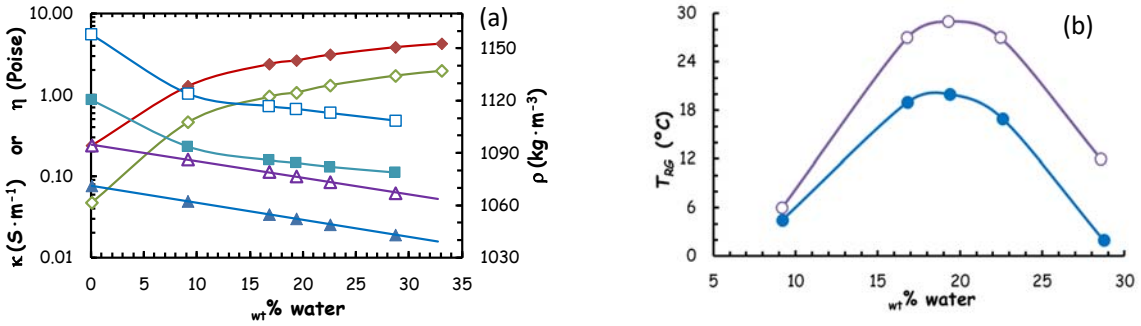

Figure 1. (a) Viscosity (squares, at left), density (triangles, at right) and ionic conductivity (rhombus, at left) at 60 °C (solid symbols) and at 25 °C (open ones) of the binary mixtures [EMIm][OSO_4] + H_2O, denoted as (n). (b) Phase transition temperature of the (n) samples without salt (solid symbols) and the (n+) samples doped to saturation with Mg sulfate salt (open ones). Composition of samples (n) and (n+) is given in in Table 2. Lines are guides for the eye.

transition). Density and viscosity have not been measured for all samples, as observed in Table 2.

Raman spectra were collected using an InVia Reflex Raman spectrometer from Renishaw. Both the 532 nm and the 785 nm laser lines were used to collect and compare spectra, although those shown in this work and further analysed by a peak fit approach were obtained by the 785 nm line of a near infrared diode laser. Together with a grating of 1,200 lines per mm, a spectral resolution better than 2 cm^{-1} was obtained. Spectra were collected at variable temperatures using a Linkam cell (THMS600) for a precise control of the temperature in the sample environment. The sample (i.e. a droplet of the mixture with a diameter of approximately 1 mm) was cooled at 5 °C/min and let to equilibrate at every temperature for 20 minutes, while the time needed to collect Raman spectra of good quality was about 10 minutes. Using a laser power of ca 100 mW, five accumulations of 10 seconds each were needed for a good signal-to-noise ratio. Finally, note that the sample is in a protective atmosphere.

Pulsed field gradient (PFG) NMR experiments were performed on a Bruker Avance 600 spectrometer at a magnetic field of 14.1 T. The spectrometer was equipped with a ^1H diffusion probe and a maximum gradient field of 1200 G·cm^{-1}. The stimulated echo pulse sequence was employed to determine the self-diffusion coefficient of the different molecular species. Diffusion measurements were performed at two different temperatures, (15 and 25 °C). The self-diffusion coefficients were obtained by fitting the decay of the echo signal with the well-known Stejskal-Tanner expression,

$$I = I_0 \cdot \exp\left\{-(\gamma\delta G)\cdot D\cdot\left(\Delta-\frac{\delta}{3}\right)\right\} \quad (1)$$

where I is the signal intensity, I_0 is the signal intensity of spin-echo at zero gradient, G is the gradient strength, D is the self-diffusion coefficient, δ the length of the gradient pulse, and Δ is the diffusion time. The applied linear gradient was varied in the range 0–200 G·cm^{-1}, while the diffusion time and the pulse duration were set to 100 and 10 ms respectively. Each experiment was based on 8 acquisitions, and the relaxation delay was set to 9 s according to the specific temperature values measured for the different samples, that were found to fall within the interval 1.30–1.75 s. The magnetic field gradient was calibrated using a standard solution of D_2O/H_2O.

Infrared spectra were recorded in the range 400 to 4000 cm^{-1} using a Bruker Vector 22 mid-infrared FT-IR spectrometer equipped with a Specac Golden Gate single-reflection diamond ATR accessory with KRS-5 optics from the UAE Unity in SAI of UDC. All data were obtained at a sample temperature of 23 °C. Spectra were processed with the Bruker Opus software package.

SAXS data for the metal-free samples were collected at the ID02 beamline at the European Synchrotron Radiation Facility (ESRF) using an instrumental setup allowing to cover Q range between 0.3 and 11 nm^{-1}. Samples were inserted into a temperature controlled flow-through cell, with internal diameter of 1.9 mm. The corresponding empty cell contribution was subtracted. Calibration to absolute units (mm^{-1}) was obtained using a neat water sample in a 2 mm capillary. For the Mg doped samples, SAXS was performed with a high-flux SAXSess camera (Anton Paar, Graz, Austria) connected to a Debyeflex 3003 X-ray generator (GE-Electric, Germany), operating at 40 kV and 50 mA with a sealed-tube Cu anode. The Goebel-mirror focused and Kratky-slit collimated X-ray beam was line shaped (17 mm horizontal dimension at the sample) and scattered radiation from the samples (measured in the transmission mode) was recorded with a one-dimensional MYTHEN-1k microstrip solid-state detector (Dectris, Switzerland), within a Q-range (with Q being the magnitude of the scattering vector) of 0.1 to 5 nm^{-1}. Copper K_α radiation of wavelength 0.154 nm was used and the sample-to-detector distance was 309 mm. This corresponds to a total 2θ region of 0.14° to 7°, applying the conversion Q (nm^{-1}) = 4π(sinθ)/λ, with 2θ being the scattering angle with respect to the incident beam and the wavelength λ of the X-rays. Samples were filled into a 2 mm (diameter) thin-walled plastic capillary tubes (polycarbonate) with vacuum-tight sealing caps at both ends. The automated temperature scan extended from 5 °C up to 50 °C in 5 °C or 10 °C steps with a waiting period of 5 minutes to allow equilibration and a subsequent exposure time of 10 min for each step. The recorded SAXS data (scattered intensities vs. scattering vector) of the samples were analysed by indexing

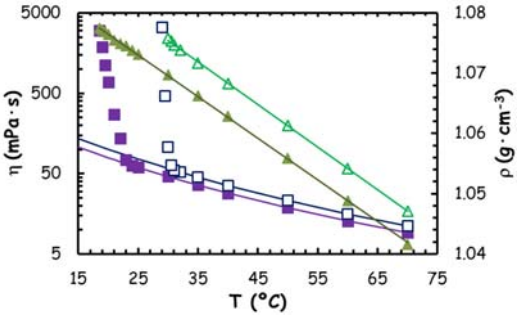

Figure 2. Viscosity (squares, at left) and density (triangles, at right) in function of temperature for the salt free (3) sample (solid symbols) and $MgSO_4$ saturated sample (3+) (open symbols). Lines are the best fit of a VTF curve for viscosity and of a straight line for density.

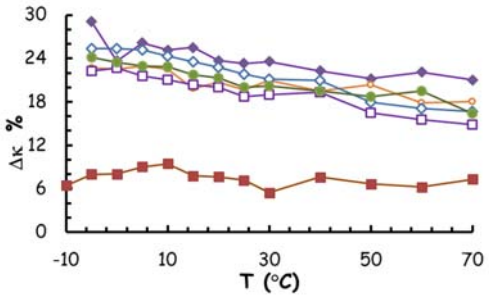

Figure 3. Ionic conductivity decreas in percentage due to $MgSO_4$ salt saturation in the six pairs of samples, (n) and (n+), given in Table 2. Solid squares correspond to (1), solid rhombus to (2), solid dots to (2.5), open dots to (3), open squares to (4) and open rhombus to (5). Lines are guides for the eye.

the diffraction peaks and extracting the lattice spacing a. In case of a 2D hexagonal lattice the expected peak positions are $Q_1 \cdot \sqrt{3}$, $Q_1 \cdot \sqrt{4}$, $Q_1 \cdot \sqrt{7}$, $Q \cdot \sqrt{9}$…, with Q_1 being the first reflection order of a hexagonal lattice, with a lattice spacing

$$a = 4\pi/(Q_1 \cdot \sqrt{3}) \quad (2)$$

and a representing the centre-to-centre distance of the hexagonal unit cells.

3. Results and discussion

3.1. Physical Properties: Water concentration influence

As previously reported, water has a profound influence on all physical properties measured in [EMIm][OSO_4], including viscosity, density, ionic conductivity and phase transition temperature, T_{RG} (defined as the temperature at which the sample does not flow under gravity (simultaneously exhibiting a huge value for dynamic viscosity, $\eta > 20$ Pa·s).).[9,25,26] The value of this last magnitude was obtained by eye for each mixture several times and the values appear in Table 2. At temperatures just above T_{RG} the sample begins to flow as a paste, passing through a stable intermediate liquid crystal phase (called quasi-gel state in Ref. 25) in a narrow range of temperatures (within 2 °C to 7 °C depending on the sample composition), before becoming completely liquid at a temperature denoted as T_G. We have observed that this intermediate state is stable at least for 24 h. In addition, we have verified that the huge viscosity value experimentally measured with the sample in intermediate state is reproduced, within the experimental errors, independently on if temperature is reached from below or above T_G. This last temperature has been obtained from the viscosity data, i.e. as the temperature where η looses its Vogel-Tamman-Fulcher (VTF) characteristic behaviour.[9] The experimentally measured viscosity and density data at $T > T_{RG}$ are included in Table S1 of the Supporting Information file, being the data for $T < T_G$ in bold case. Also, in Table S2 we include data of the ionic conductivity for all of the binary aqueous samples (n) studied.

The influence of the water on viscosity on viscosity, density and ionic conductivity of the aqueous mixtures (n) 25 °C and 60 °C is shown in Figure 1(a). Viscosity decreases exponentially with the water content, while density decreases linearly. In contrast ionic conductivity increases exponentially with water content. These results are in accordance with the behaviour of other IL+water mixtures previously studied.[4,9,24-27] Note that the inverse proportionality between ionic conductivity and viscosity that we observe in this IL is in full agreement with the predictions of Walden's rule.[8,25]

Figure 1(b) shows T_{RG} values for (n) samples, which present a bell-shape (solid dots at left axis) with a maximum at about 20 $_{wt}$% of water, which corresponds to $x_{IL} \approx 0.2$. These results also agree with previous measurements.[9,25] Note that samples (0) and (5) do not form any liquid crystalline phase. Hence, the novel aspect studied here will be understanding the influence that Mg-doping may have on these mixtures.

3.2. Physical Properties: Magnesium salt influence

Viscosity and density values measured for samples (3) and (3+) are plotted in Figure 2 as a function of temperature, the corresponding data being available also in Table S1. Upon addition of the salt, both viscosity and density increase, as was also observed upon addition of univalent salts.[24] T_{RG} increases by up to 10 °C in the Mg-doped samples respecting the no doped ones as shown in Figure 1(b). In addition, $MgSO_4$ narrows the temperature range of the intermediate

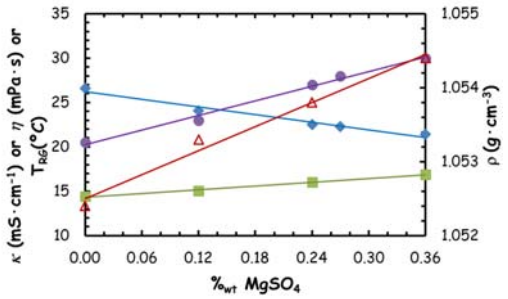

Figure 4. Ionic conductivity (rhombus, at left), viscosity (squares, at left) and density (triangles, at right) for the (2.5a/b) samples at 60 ºC, and phase transition temperature (dots, at left), in function of weight percentage of the magnesium sulfate salt. Curves are the best fit of a straight line.

state, as observed in Figure 2, where T_G and T_{RG} for the two samples are marked. Note that this range (equal to T_G - T_{RG}) diminishes from about 7 °C for sample (3) to only 3 °C for sample (3+). Figure 2 shows that density decreases linearly with temperature (triangle symbols referred to right axis), and that the salt addition increases density values without affecting the linear dependence on T (which is about −0.7 kg·m^{-3}·K^{-1}). The increase of mass due to the salt addition, even assuming that the molar volume of sample (3) does not change, cannot justify the increase of the density value. Thus, it must be assumed that ionic packing is favoured by the addition of $MgSO_4$.

The ionic conductivity experimental data for the doped (n+) samples are included in Table S2. As observed κ-value decreases as a result of $MgSO_4$ salt addition. The conductivity loss, in percentage ($\Delta\kappa\%$) is defined as,

$$\Delta\kappa\% = 100\,\frac{\kappa_{(n)}-\kappa_{(n+)}}{\kappa_{(n)}} \qquad (3)$$

Except for the sample (1) (which has the lowest quantity of water) the percentage of the ionic conductivity decrease is almost independent of the water content, as shown in Figure 3. Also, $\Delta\kappa\%$ decreases slightly with temperature for all mixtures, ranging from about 25 % at −5 °C to about 18 % at 70 °C (except again for sample (1) which percentage decrease is about 7.5 % independently of temperature).

Next, we are going to analyse the influence of the Mg salt concentration in the studied physical properties. As explained in Section 2, we mixed samples (2.5) and (2.5+) in different proportions to obtain five samples (including the saturated mixture and the salt free one) with increasing Mg content, which composition appears in Table 2. In Figure 4 we plot the obtained values of η (square at left), ρ (triangles at right) and κ (rhombus at left) for those five samples at 60 °C (to have all of them in liquid state), and also T_{RG} (dots at left axis). As observed the dependence of all properties is roughly linear with the salt content, so we can tune it adding the optimal salt quantity.

3.3. Raman Spectroscopy

Figure 5 shows the Raman spectrum of a [EMIm][OSO_4] aqueous mixture, sample (3), obtained at 30 °C with the 785 nm laser line as the excitation source. The vibrational modes of the $[SO_4]^{2-}$ group of the octylsulfate as well as of the –CH group of the imidazolium ring (cation) and of the alkyl chain of the

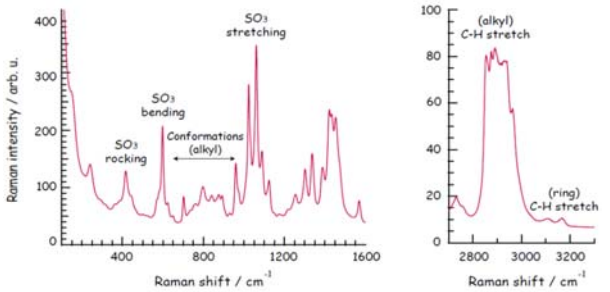

Figure 5. Raman spectrum of sample (3) recorded at 30 °C. See Table 2 for sample composition.

Table 3. Vibrational frequencies of selected vibrational modes and their proposed assignment according to previously reported works

Wave number	Assignment	Reference
580 cm^{-1}	–SO deformation	[28,29]
598 cm^{-1}	in-plane ν N–CH_3 stretch $[EMIm]^+$	[30]
798 cm^{-1}	ν CO–S or ν C–OS	[31] Or [32]
960 cm^{-1}	ν C–C ($C_2C_1Im^+$)	[30,33,34]
977 cm^{-1}	ν S–OC or gauche isomers in alkyl chain	[29,35] or [36]
1060 cm^{-1}	S–O_3^- stretch	[31,32,37]
2800–3000 cm^{-1}	C–H stretch (alkyl)	[38,39]
3112 cm^{-1}	C^2–H stretch (ring)	[40,41]
3163 cm^{-1}	$C^{4,5}$–H stretch (ring)	[40,41]

octylsulfate anion are observed at distinct frequency ranges. A full assignment of these vibrational modes based on precedent studies is given in Table 3.[28-41]

The Raman spectrum of the sample (3+) is very similar to that of sample (3) (see Figure S1 in the supplementary Information for a comparison of both spectra) since the low concentration of the added salt (even at saturation, as observed in Table 2) does not result in strong signatures from the additional $[Mg]^{2+}$ and $[SO_4]^{2-}$ ions.

Upon cooling, which drives the sample into a liquid crystalline state, the Raman spectra of sample (3+) show clear changes in the position and/or intensity of the characteristic vibrational modes, as shown in Figure 6. More precisely, the deformation modes at 570 and 580 cm^{-1} become narrower and increase in intensity, Figure 6(a), the intensity of the symmetric S–O stretch decreases compared to other proximate vibrations, Figure 6(b), while the C–H stretch vibrations show a relative intensity change in the alkyl chain, Figure 6(c), and both intensity and frequency change in the imidazolium ring, inset of Figure 6(c). All these changes were also detected in the binary mixture sample (3), as summarized in Figure S2 in the Supplementary Information file. The symmetric S–O stretching mode is the strongest signature in the recorded Raman spectra, due to the symmetry of this vibration and thus a large change in polarizability. The frequency of this mode is known to be a strong indication of the association state of $–SO_4$ containing anions, shifting to higher frequencies in the case of ion-pairs or larger ionic aggregates, while lower frequencies are observed for more free anions in association to for instance bulky cations.[28] A deeper analysis of Figure 6(b) reveals that this mode shifts by less than 1 cm^{-1} upon decreased temperature from 32 °C to 5 °C, and that its intensity decreases slightly upon cooling. Altogether, this behaviour indicates a change in the local geometry (anion-cation-water relative positions) rather than in the strength of ionic association or H-bonding.

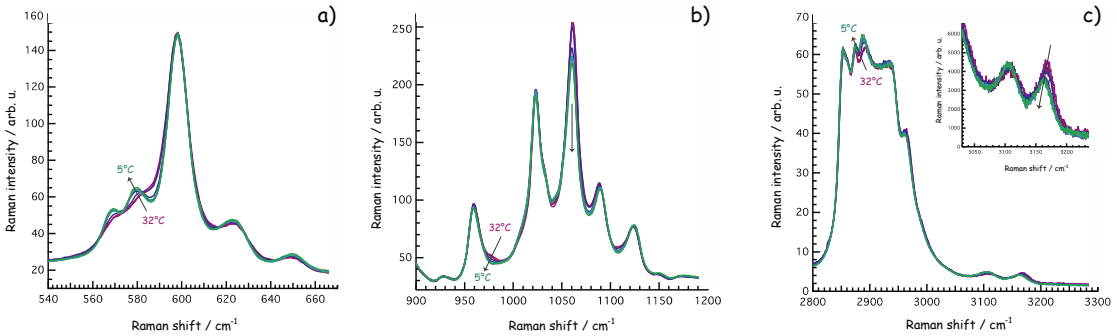

Figure 6. Selected regions of the Raman spectra recorded for sample (3+) at 30 °C (liquid phase) and 5 °C (rigid gel phase).

In addition, the 2800–3000 cm^{-1} region shows that when the sample cools (and thus becomes a liquid crystal) the intensity of the peak at 2885 cm^{-1} (asymmetric C–H_2 stretch) slightly increases with respect to the one at 2850 cm^{-1} (sym. C–H_2 stretch), Figure 6(c), an observation that has previously been used as an indication of increased chain packing and decreased chain mobility.[29] The small but detectable downshift in frequency and increase in intensity of the mode at 2885 cm^{-1} upon cooling can thus be attributed to reduced chain rotations around the chain axis and increased chain-chain interactions. To get a better understanding of these spectral changes a peak fit analysis has been employed using a set of Lorentzian functions and a linear background, as shown in Figure 7 for the representative case of sample (3+) (see also the Supplementary Information file). This approach reveals a more precise temperature dependence of the spectral changes and in particular more pronounced peak frequency shifts and peak narrowing effects at a temperature of 25 °C. This temperature is in perfect agreement with the transition temperature determined from light microscopy and viscosity measurements and previously attributed to an isotropic-mesomorphic phase transition.[9,25] In Figure 7(a) it is observed that the C–H stretching modes of the imidazolium ring found at 3112 cm^{-1} (ν C^2–H) and at 3163 cm^{-1} (ν $C^{4,5}$–H) show a red shift in frequency upon cooling, indicating the experience of stronger H–bonds by the $C^{2,4,5}$H groups. In addition, the vibrational modes associated to the C^2–H stretch get narrower than the $C^{4,5}$–H counterpart, suggesting that on cooling the –C^2H group on the ring becomes a preferred site of interaction. Also, Figure 7(b) shows that the two peaks associated to the –SO deformation at 570 and 580 cm^{-1} become narrower, which is in contrast to the peak width of the N–CH_3 stretching mode of the cation observed at 598 cm^{-1} that is much less affected by the temperature decrease. To summarize, the results obtained by Raman spectroscopy indicate a structural transition upon cooling that involves both anion-cation and water-ion interactions, as will be discussed later in further details.

3.4. Diffusion NMR

Figure 8 shows the relationship between the self-diffusion coefficient measured for the cation (D_{cation}) and for the anion

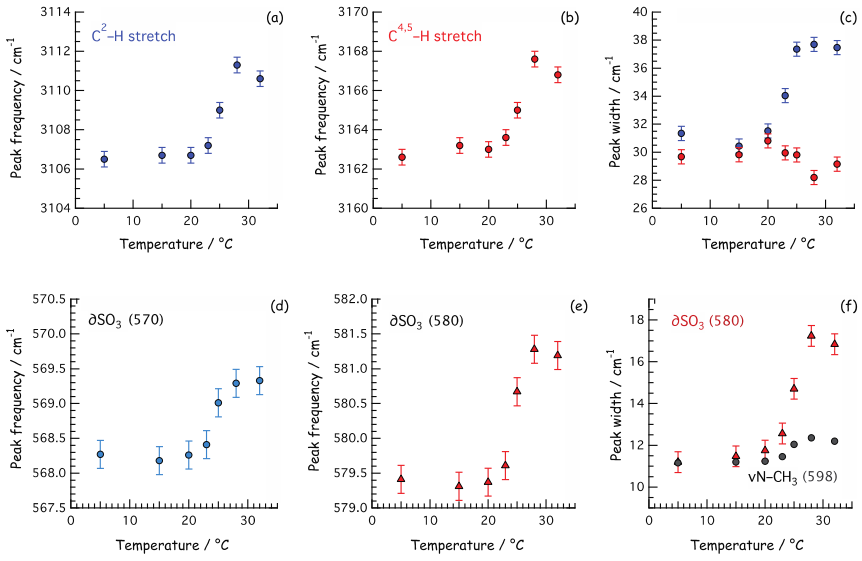

Figure 7. Results from the peak fit analysis of selected regions of the Raman spectra recorded at variable temperatures for the sample (3+).

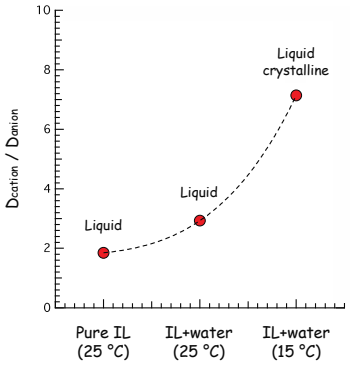

Figure 8. Ratio between the self-diffusion coefficients of the cation and the anion for the pure IL (at 25 °C), and the water/IL mixture at both 25 and 15 °C.

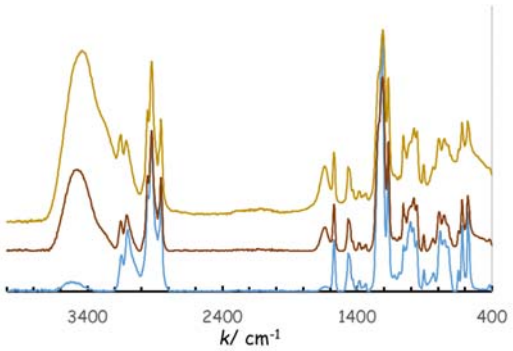

Figure 9. FTIR spectra for samples (0), blue line at bottom; sample (3), brown line in the middle, and sample (3+), yellow line in the top. Samples composition is given in Table 2.

(D_{anion}) at different compositional or thermal conditions. These values were obtained by fitting the decay of the echo signal with the well-known Stejskal-Tanner expression, Equation (2) (the original values are also given in Table 4). Figure 8 shows that in the pure ionic liquid the diffusivity of the cation is twice that of the anion at 25 °C, and about three times that of the anion upon addition of water. However, at 15 °C, the temperature at which the mixture is in the liquid crystalline state, the cations move seven times faster than the anion. This is in nice consistency with the mesomorphic phase structure shown below, where anions are supposed to be rigidly bound by H-bonds while the cations are more mobile by experiencing a water-rich domain.

3.5. Infrared spectroscopy

Figure 9 displays the infrared spectra recorded for sample (0) (blue line at bottom), sample (2) (brown line in the middle) and sample (3+) (yellow line at top), vertically offset for a better visualization. Spectral features characteristic of the $[EMIm]^+$ cation (ring stretching at wavenumber 1570 cm^{-1} and bending at 1450 cm^{-1}),[42] and the sulfate anion (stretching at k = 1160 and 990 cm^{-1}, and bending at 600 cm^{-1}) are observed.[43] In addition, the vibrational modes of water (1650 cm^{-1} for bending and 3500 cm^{-1} for stretching)[44] are also observed. In Figure 10 we show in greater details three regions with the spectra normalized to the base line to emphasize intensity differences. Thus, in Figure 10(a) two characteristic peaks corresponding to the $[EMIm]^+$ cations are observed, with comparable position and intensities. In Figure 10(b) peaks corresponding to the $[SO_4]^{2-}$ anion show differences in the relative height of each, mainly from the pure sample (blue line) and the aqueous mixed ones. This reveals a change in the different modes of the sulfate anion due to the presence of water because the height of a peak is related with the number (or strength) of that interaction. The addition of the Mg sulfate does not change appreciably the position of these peaks or its relative height. Finally, in Figure 10(c) we show in detail the peak corresponding to water stretching, including that of pure H_2O as a black line. The water content is reflected by the intensity of that peak (that of pure water has been divided by 5), while the position reflects the number of H-bonds formed, which are typically manifested by a red-shift.[44] The red-shift observed upon addition of the salt, indicates stronger H-bonds with respect to both the nearly dry (0) and the salt-free (2) samples.

Table 4. Diffusion coefficient values for cation and anion from NMR for sample (0) and sample (3), this last in both phases, liquid (at 25 °C) and liquid crystal (at 15 °C). See Table 2 for sample compositions.

Sample (temp., state)	D_{cation} (C^2**H**)	D_{cation} ($C^{4,5}$**H**)	D_{anion} (C**H**$_3$)	D_{cation}/D_{anion}
(0) (25 °C, liquid)	4.51 $\mu m^2/s$	4.57 $\mu m^2/s$	2.45 $\mu m^2/s$	1.85
(3) (25 °C, liquid)	88.8 $\mu m^2/s$	91.5 $\mu m^2/s$	30.7 $\mu m^2/s$	2.93
(3) (15 °C, liq. crystal)	52.6 $\mu m^2/s$	49.0 $\mu m^2/s$	7.12 $\mu m^2/s$	7.14

3.6. Small Angle X-ray Scattering (SAXS)

Let's first analyse the SAXS data obtained from the aqueous mixtures of $[EMIm][OSO_4]$ from high dilution, x_{IL} = 0.003 (about 95 $_{wt}$% of water) to medium diluted ones, x_{IL} = 0.343 (about 10 $_{wt}$% of water). The resulting curves are shown in Figures 11(a) and (b), after subtraction of the empty cell contribution. Data in Figure 11(a) refer to the concentration range from x_{IL} = 0.003 to 0.049. In the more dilute regime (dashed lines; $x_{IL} \leq 0.014$), the scattering curves resemble similar data sets from aqueous solutions of other alky sulfate-based salts, such as sodium dodecyl sulfate.[45-48] Similarly to other cases, these data can be described as originating from core-shell ellipsoidal micelles, whose sizes remain approximately constant, as witnessed by the invariance of the minimum position at ca. Q = 1.3 nm^{-1} indicated by the dashed line in Figure 11(a). At larger IL content

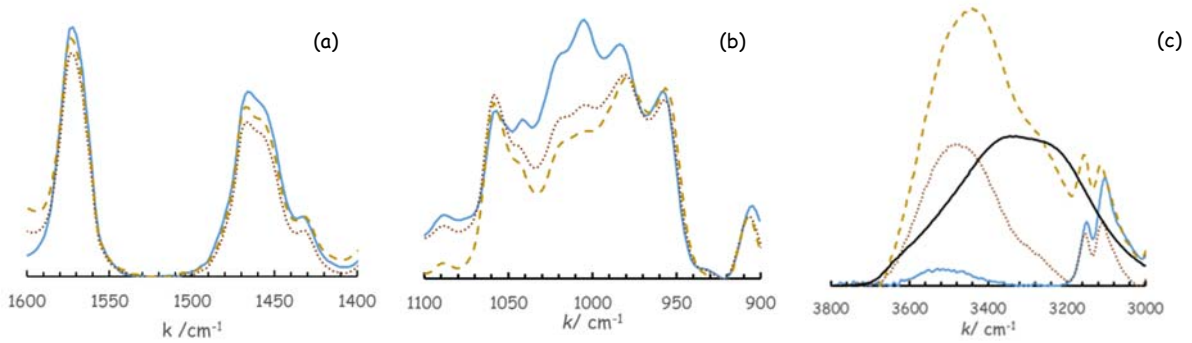

Figure 10. Selected regions of FTIR spectra normalized for samples (0), continuous blue line; sample (2), doted brown line, and sample (3+), shaded yellow line: a) Region of [EMIm] peaks. b) Region of sulfate peaks. c) Peak for water stretching (including pure water given by black line. Samples composition is given in Table 2.

(continuous lines; $x_{IL} > 0.014$), a structural transition is observed as demonstrated by the low shift of the minimum, centred at ca. 1.3 nm^{-1}, and the growing of a form factor peak at ca. 1.7 nm^{-1}, resulting from the formation of a cylindrical structure. We note that this transition occurs in a concentration range comparable to that reported by Kumar and co-authors for changes of properties like speed of sound and conductivity in aqueous solutions of 1-butyl-3-methyl imidazolium octylsulfate, or [BMIm][OSO_4].[49]

In Figure 11(b) data for IL-richer mixtures are shown, where the concentration ranges from x_{IL} = 0.10 to 0.343 (data for neat [EMIm][OSO_4], sample (0), are also included). It appears that together with an amorphous halo centred at ca. Q = 2 nm^{-1}, also sharp Bragg peaks are present in the concentration range $0.2 \leq x_{IL} \leq 0.26$ at room temperature. We note that the mentioned amorphous halo is present also in sample (0) and it has been related to structurally segregated alkyl tails in the neat sample, similarly to a plethora of other ILs.[17,50-52] The Bragg peaks are a more uncommon feature, as they evidence the formation of a liquid crystalline phase.[14,53,54]

These diffraction features, that seem to correlate to the complex behaviour detected by the other techniques, were further analysed as a function of temperature, between -40 °C and +30°C, for sample (2.5), see Figure 12. It appears that data above 23 °C show just an amorphous halo at Q = 2.38 nm^{-1} (indicative of the mesophase), but upon cooling additional and narrower Bragg peaks develop. Using a temperature resolution of 2 °C, we identified the temperature at which the appearance of the Bragg peaks occurs, which agrees within the experimental errors with that where the intermediate crystal liquid phase, obtained from viscosimetry, appears at T_G.[9,25] In order to extract additional information from Figure 12, we observe the presence of three Bragg peaks (at 2.18, 3.78 and 5.77 nm^{-1} for 0 °C. These peaks can be indexed to a columnar hexagonal structure 1:√3:√7 (peak at √4 is missing). As known, hexagonal mesophases consist of densely packed cylindrical micelles that are organised into a 2D hexagonal lattice. The lattice parameter a, i.e. the distance between the centres of adjacent cylinders, is given by Equation (1), where Q_I is the principal peak position.[55] Based on this definition, we show in Figure 13 the concentration and temperature dependence of the lattice parameter a for selected samples. It can be noticed that at any given temperature in lyotropic crystalline regime, increasing the IL content leads to a decrease of a, which in all cases is of the order of several nm.

These results indicate that upon increasing the IL concentration, a progressive transition from ellipsoidal micelles to cylindrical ones occurs and eventually the latter will tend to lead to a 2D hexagonal lattice. Further increase of the IL content will lead to a strong change of organization, leading to 2D hexagonal packing of the cylindrical aggregates. This dramatic change in organization is responsible for the sudden increase in viscosity, while maintaining properties such as density or ionic conductivity unaltered.

The influence of adding $MgSO_4$ on the SAXS patterns is shown in Figure 14. Figure 14(a) shows a broad correlation peak for sample (0), whose position remains constant over the temperature range investigated. This indicates an isotropic fluid phase over the entire temperature range, with a correlation distance of a = 2.51 nm. This single broad correlation has been attributed to structurally segregated alkyl chains (*vide supra*).[50-52] The SAXS data of sample (3) for a range of temperatures are shown in Figure 14(b), while those corresponding to sample (3+) appear in Figure 14(c). Both exhibit the scattering pattern of a hexagonal phase at low temperatures, with a phase transition to an isotropic fluid phase above 25 °C for sample (3) and above 30 °C for sample (3+). In Figure 14(b) we can observe that at 20 °C the SAXS data for sample (3) reveal that it is in the intermediate liquid crystalline state, which does not appear in Figure 14(c) (due to the temperatures studied). The lattice spacing a is 3.14 ± 0.02 nm at 5 °C and 3.10 ± 0.02 nm just before the phase transition. The isotropic fluid above T_G again shows a broad peak at $Q \approx 2.5$ nm^{-1}, similar to that of sample (0). Again we observe that at temperatures below 25 °C in sample (3), and below 30 °C in sample (3+), the formation of an ordered 2D mesophase with a defined hexagonal lattice appears.

3.7. Polarised microscopy

As an additional confirmation of the phase transitions, we have taken some micrographs by cross polarized microscopy, with an

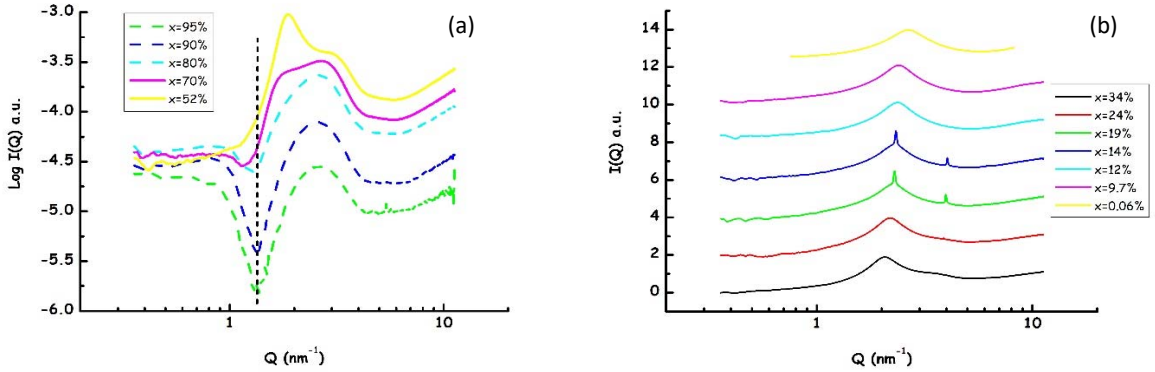

Figure 11. (a) Small Angle X-ray Scattering data from mixtures of [EMIm][OSO_4] and water in the dilute regime. Dashed lines refer to concentrations lower than x_{IL}= 0.014. The dashed vertical line indicates the invariance of the minimum position for the dilute mixtures, fingerprinting the invariance of characteristic sizes of the core-shell elliptical aggregates. (b) SAXS data from mixtures of [EMIm][OSO_4] and water at concentration above x_{IL}= 0.1. In both Figures, the legends report the water content in $_{wt}$%.

area of 400 x 290 µm^2. When the sample is in the isotropic liquid state no light passes. In contrast, when sample is in the lyotropic liquid crystalline state we can observe clearly the typical optical textures reported for these mesophases.[56] Similar micrographs have been already published for other polymeric ILs in their quasi-solid state.[57] The structure is strongly affected by boundary effects as can be seen in Figure 15, where the left image was taken for a droplet deposited over a glass substrate while the right image was taken for a sample sandwiched between two glass plates.

In Figure 16 we present a micrograph recorded for sample (2.5+) at room temperature (hence in the liquid crystalline state). They were made with a confocal microscopy with white polarized light. Structures longer than 100 µm and with diameters of some µm are observed, formed by aggregation of thinner cylindrical structures. The origin of these microstructures must be attributed to $MgSO_4$ crystals not dissolved in the bulk of the sample, in spite of the fact that they resemble those of the H_I liquid crystal phase proposed for the mixtures. Unfortunately, this last mesostructure cannot be seen with optical microscopy.

4. Structure of the mesomorphic phase

To explain the experimental facts described in the previous sections, we have proposed a mesostructure model for the binary aqueous mixture behaviour that schematically appears in Figure 17.[25] The formation of the mesomorphic liquid crystalline state is triggered by water molecules interacting through H-bonds with the oxygen atoms of the octyl sulfate anion (being the most effective 4 water molecules per sulfate anion, i.e. a water molecule per sulfate oxygen, which means x_{IL} ≈ 0.2). The amphiphilic character of the anion results in the formation of micelles with the tails in the core and the sulfate head at the surface, which are H-bonded to water molecules. The chromonic character of [EMIm] cation would generate tubular micelles, being placed in the mantle of them,[58] only

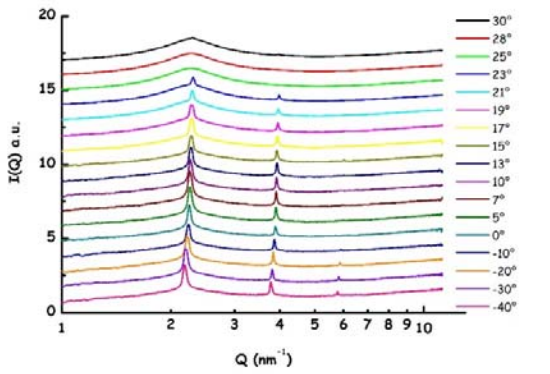

Figure 12. Temperature dependence of SAXS pattern from the sample (2.5). Data are vertically offset for the sake of clarity.

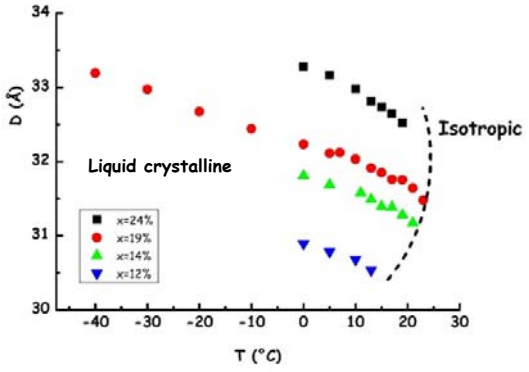

Figure 13. Lattice parameter a for the mixtures of [EMIm][OSO_4] and water with 0.15 < x_{IL} < 0.29, as a function of temperature obtained from the analysis of the SAXS patterns. The resultant phase diagram indicates that at high enough temperature, only micellar aggregates can be detected. At low temperatures, the formation 2D hexagonal lattice occurs.

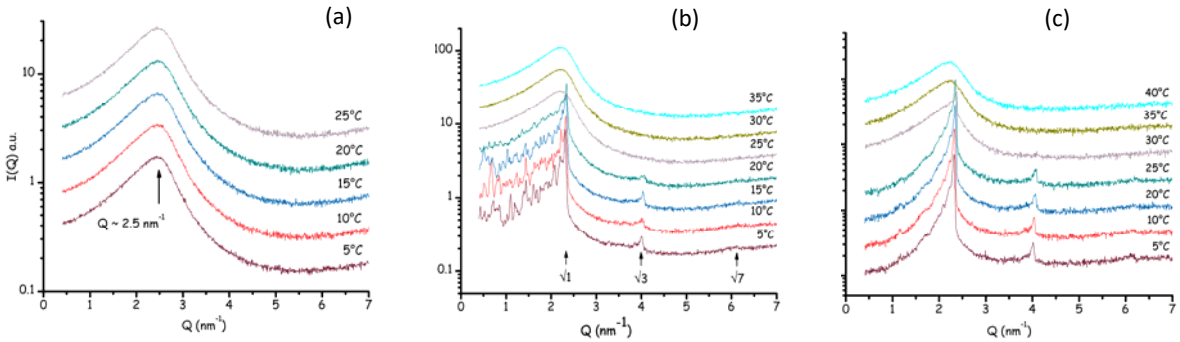

Figure 14. SAXS patterns (logarithmic scattering intensities I vs. Q) of: (a) sample (0), (b) sample (3) and (c) sample (3+), at different temperatures in a heating scan from 5 °C to 25°/35°/40°C in 5 or 10 °C steps. The plots during the T-scans are shifted vertically for better visibility. The arrows mark the expected peaks for a 2D-hexagonal lattice. It should be noted that the √4 peak is extinct, most probably caused by the form factor of the hexagonal unit-cell being coincidently null at this Q-position.

weakly connected with the anions due to the water film between both ions. Thermal motion will prevent micelle association, which occurs in a hexagonal H_I fashion when temperature diminishes, giving place to the lyotropic liquid crystalline phase. Diffusion of $[EMIm]^+$ cations on these cylindrical micelles network would be much easier than anion diffusion. Thus, charge transport would be mainly due to the cations, with the same ionic density and velocity in isotropic and mesomorphic states (deduced from the absence of any transition at T_{RG} for κ). A similar mechanism of charge transport has been recently proposed to explain ionic conduction in quasi solid poly ionic liquids.[24] When the magnesium sulfate is added to the aqueous solutions, the metal cations are solvated in the water-$[OSO_4]$ network forming solid nanodomains in the polar region, which would increase viscosity in liquid state and also reduce the network motion (which increases T_{RG}).

This nanostructure has been recently observed by some of us from molecular dynamics simulations for univalent[6,59-61] and divalent metals[62] although for ILs that do not form mesomorphic state. In this last reference we observed that divalent cations will generate a more ordered structure than univalent ones, which could explain the higher T_{RG} increase obtained for the Mg doped sample respecting those doped with univalent salts.[25] The $[SO_4]$ anions would coordinate with [EMIm] cations in the wall of the tubular micelles, so decreasing the number of them free to transport charge (which would decrease the conductivity). That effect would explain why the decrease of ionic conductivity is the same for all samples, independently of the water (and $MgSO_4$) content observed in Figure 3. This mesostructure picture is substantiated through the Raman spectroscopy results described above, where we observed that, when water is added the $[OSO_4]$ head group is expected to H-bond to water, these H-bonds being more or less symmetric around the anionic group. The new vibrational mode observed at 977 cm^{-1}, shown in Figure 8(b), is thus tentatively assigned to H-bound S-O_3 groups, due to the frequency being intermediate between that of fully dissociated S-O_3^- groups (1061 cm^{-1}) and that of a S-OH group (890–900 cm^{-1}).[63] Upon cooling these H-bonds become stronger, the chains interact more strongly and some water molecules are pulled out to the ionic region. This geometry change can explain the loss in Raman intensity for the S-O_3 stretching mode (at 1061 cm^{-1}), the red shift of the S-O···H modes (970 cm^{-1}), and consequently suggest that the cation can keep its high dynamics because it has more water molecules around while the anion is glued in place by both van der Waals forces (in the non-polar domains) and H-bonds (in the polar domain). The self-diffusion ratio between cation and anion shown in Figure 10 demonstrates that charge transport is mainly due to cations, both in the liquid and, as more evident, in the liquid crystalline state. This charge

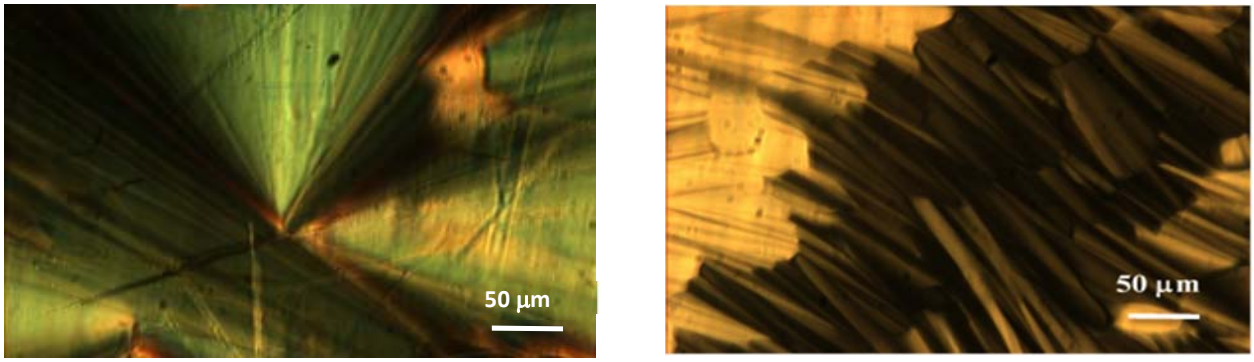

Figure 15. Micrographs of the sample (3+) in liquid crystalline state obtained by cross polarizing microscopy. At left a drop, and at right, same sample in a sandwich.

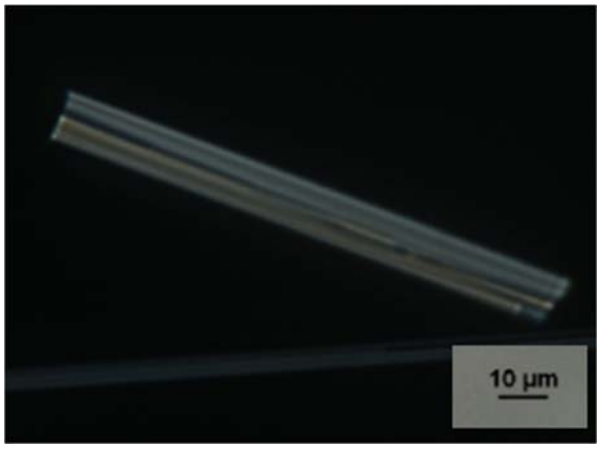

Figure 16. Confocal micrographs made with white polarized light of sample (2.5+) in liquid crystalline state showing a $MgSO_4$ crystal not dissolved.

transport mechanism resembles that observed in 1D channels suggested for nanostructured columnar liquid crystals.[64] In spite of the fact that the systems and scales are different, the mesostructure in columnar H_I hexagonal pattern is very similar. SAXS results are also consistent with the above given picture and can be explained if mesostructrure consists of micellar rods with a central hydrophobic core arranged in a regular 2D hexagonal lattice surrounded by water in the interstitial space between the neighbouring rods (H_I-phase). Upon heating, a phase-transition occurs at T_{RG} to an isotropic fluid phase, where the long-range order of the hexagonal lattice is lost. However, a short-range local order is maintained, being in a range similar to that of the hexagonal lattice, which is indicated by approximately the same *Q*-position of the broad correlation peak in the SAXS pattern. The T_{RG} is up to 10 °C higher with $MgSO_4$ than without it, probably because the higher stability of the lattice structure due to the hydration of the Mg^{2+} ions.

5. Conclusions

In this paper, we show the H_I mesostructure of the aqueous mixtures of the ionic liquid [EMIm][OSO_4]. Also, we study the influence on that mesostructure and their physical properties of the $MgSO_4$ salt addition in the mixture. The mesostructure proposed is in agreement with results obtained from SAXS, infrared, Raman and diffusion NMR for samples in the liquid and the mesomorphic state. The mesomorphic structure can be observed through polarized microscopy. Finally, some of the Mg-doped samples in the liquid crystalline phase present a relatively high ionic conductivity at room temperature. This indicates that the mixtures studied here are potential quasi-solid electrolytes based on Mg ions as smart materials for electrochemical devices.

Conflicts of interest

There are no conflicts to declare

Acknowledgements

The authors are grateful to the technician M. Cabanas for some of the great quality measurements and also to UEM, UEPM and UM of SAI from UDC. This work was supported by MINECO from Spanish Government (Grants No. MAT2014-57943-C3-1-P, MAT2014-57943-C3-2-P and MAT2014-57943-C3-3-P), COST program Action CM 1206 EXIL, and by the Xunta de Galicia through the research projects Network on Ionic Liquids, REGALIs (CN 2014/015), AGRU 2015/11 and GDR ED413C 2016/001. Research projects have been co-financed by the European Regional Development Fund (FEDER). A.M. and N. Y. acknowledge the financial support from the ÅForsk Foundation in Sweden (grant nº 16-644, 2016). We also acknowledge the European Synchrotron Radiation Facility for provision of synchrotron radiation facilities and would like to thank Dr. E. Di Cola and T. Narayanan for their kind and competent assistance in exploiting beamline ID02.

Notes and references

1 R. D. Rogers and K.R. Seddon (Eds.), Ionic Liquids, Industrial Applications to Green Chemistry, ACS Symp. Series 818, Am. Chem. Soc., Washington, 2002.
2 H. Ohno (Ed.), Electrochemical aspects of Ionic Liquids, Wiley and Sons, New Jersey, 2011.
3 M. Armand, F. Endres, D.R. MacFarlane, H. Ohno and B. Scrosati, Nat. Mat., 2009, 8, 621.
4 J. Vila, P. Ginés, J.M. Pico, C. Franjo, E. Jiménez, L.M. Varela and O. Cabeza, Fluid Ph. Equilibria, 2006, 247, 32.

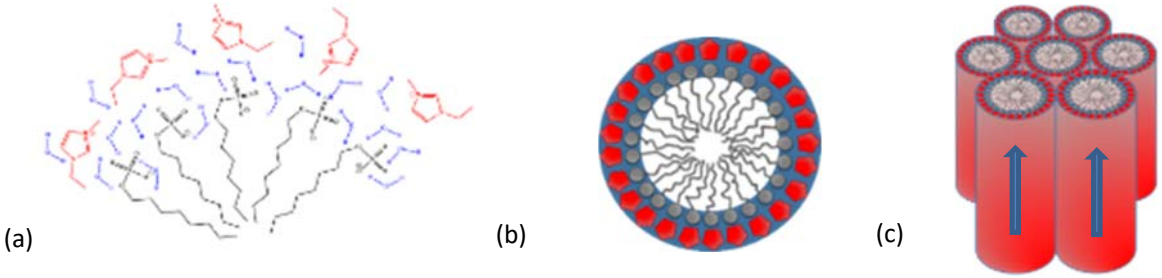

Figure 17. (a) Schematic scheme of the nanostructure of the aqueous mixture of [EMIm][OSO_4]. (b) Tubular section, red pentagons correspond to [EMIm] cation, grey dot with a tail to [OSO_4] anions and blue is for water. (c) Hexagonal tubular H_I mesostructure formed, giving place to 1D ionic conduction.

5 F. Endres, ChemPhysChem, 2002, 3, 144.
6 L. M. Varela, T. Méndez-Morales, J. Carrete, V. Gómez-González, B. Docampo-Álvarez, L. J. Gallego, O. Cabeza and O. Russina, J. Mol. Liq., 2015, 210, 178.
7 S. A. M. Noor, P. C. Howlett, D. R. MacFarlane and M. Forsyth, Electrochimica Acta, 2013, 114, 766.
8 S. García-Garabal, J. Vila, E. Rilo, M. Domínguez-Perez, L. Segade, E. Tojo, P. Verdía, L. M. Varela and O. Cabeza, Electrochimica Acta, 231 2017, 231, 94.
9 O. Cabeza, J. Vila, E. Rilo, M. Domínguez-Pérez, L. Otero-Cernadas, E. López-Lago, T. Méndez-Morales and L. M. Varela, J. Chem. Thermodyn., 2014, 75, 52.
10 S. T. Hyde, Handbook of Applied Surface and Colloid Chemistry, 2002, 2, 299.
11 J. Fu, Y. I. Yang, J. Zhang, Q. Chen, X. Shen and Y. Q. Gao, J. Phys. Chem. B, 2016, 120, 5194.
12 T. Inoue, H. Ebina, B. Dong and L. Zheng, J. Colloid Interface Sci., 2007, 314, 236.
13 M. Figueira-González, V. Francisco, L. García-Río, E. F. Marques, M. Parajó and P. Rodríguez-Dafonte, J. Phys. Chem. B, 2013, 117, 2926.
14 M. A. Firestone, J. A. Dzielawa, P. Zapol, L.A. Curtiss, S. Seifert and M. L. Dietz, Langmuir, 2002, 18, 7258.
15 H. Kaper and B. Smarsly, Z. Phys. Chem., 2009, 220, 1455.
16 O. Russina, L. Gontrani, B. Fazio, D. Lombardo, A. Triolo and R. Caminiti, Chem. Phys. Lett., 2010, 493, 259.
17 O. Russina and A. Triolo, Faraday Discuss., 2012, 154, 97.
18 O. Russina, F. Lo Celso, N. V. Plechkova and A. Triolo, J. Phys. Chem. Lett., 2017, 8, 1197.
19 A. Noda and M. Watanabe, Electrochim. Acta, 2000, 45, 1265.
20 P. Vidinha, N. M. T. Lourenço, C. Pinheiro, A. R. Brás, T. Carvalho, T. Santos-Silva, A. Mukhopadhyay, M. J. Romaô, J. Parola, M. Dionisio, J. M. S. Cabral, C. A. M. Afonso and S. Barreiros, Chem. Commun., 2008, 44, 5842.
21 S. Doherty, J. G. Knight, J. R. Ellison, P. Goodrich, L. Hall, C. Hardacre, M. J. Muldoon, S. Park, A. Ribeiro, C. A. Nieto de Castro, M. J. Lourenço and P. Davey, Green Chem., 2014, 16, 1470.
22 N. Yoshimoto, T. Shirai and M. Morita, Electrochim. Acta, 2005, 50, 3866.
23 M. Cai, Y. Liang, F. Zhou and W. Liu, J. Mater. Chem., 2011, 21, 13399.
24 A. S. Shaplov, R. Marcilla and D. Mecerreyes, Electrochim. Acta, 2015, 175, 18.
25 O. Cabeza, L. Segade, M. Domínguez-Pérez, E. Rilo, S. García-Garabal, D. Ausín, A. Martinelli, E. López-Lago and L. M. Varela, J. Chem. Thermodyn., 2017, 112, 267.
26 E. Rilo, L.M. Varela and O. Cabeza, J. Chem. Eng. Data, 2012, 57, 2136.
27 O. Cabeza, S. García-Garabal, L. Segade, M. Domínguez-Pérez, E. Rilo and L. M. Varela, Ionic Liquids: Theory, properties, new approaches (Ed. A. Kokorin) pp. 111, Ed. In Tech. Vienna, 2011.
28 J.R. Hall and R.A. Johnson, J. Raman Spectrosc., 1981, 11, 279.
29 M. Picquart, J. Phys. Chem., 1986, 90, 243.
30 J. Grondin, J.-C. Lassègues, D. Cavagnat, T. Buffeteau, P. Johansson and R. Holomb, J. Raman Spectrosc., 2011, 42, 733.
31 V. B. Kartha, L. C. Leitch and H. H. Mantsch, Can. J. Chem., 1984, 62, 128.
32 M. H. Brooker, J. Chem. Soc., Faraday Trans., 1984, 80, 73.
33 J. C. Lassegues, J. Grondin, R. Holomb and P. Johansson, J. Raman Spectrosc., 2007, 38, 551.
34 Y. Umebayashi, T. Fujimori, T. Sukizaki, M. Asada, F. R. Kanzaki and S. Ishiguro, J. Phys. Chem. A, 2005, 109, 8976.
35 G. Cazzolli, S. Caponi, A. Defant, C. M. Gambi, S. Marchetti, M. Mattarelli, M. Montagna, B. Rossi, F. Rossi and G. Viliani, J. Raman Spectrosc., 2012, 43, 1877.
36 T. Ikeda, T. Yoshida and H. Okabayashi, Z. Naturforsch., 1983, 38a, 1046.
37 M. C. C. Ribeiro, J. Phys. Chem. B, 2012, 116, 7281.
38 M. N. Garaga, M. Nayeri and A. Martinelli, J. Mol. Liq., 2015, 2015, 169.
39 A. M. Moschovi, V. Dracopoulos and V. Nikolakis, J. Phys. Chem. B, 2014, 118, 8673.
40 S. Cha, M. Ao, W. Sung, B. Moon, B. Ahlström, P. Johansson, Y. Ouchi and D. Kim, Phys Chem Chem Phys, 2014, 16, 9591.
41 N. Yaghini, J. Pitawala, A. Matic and A. Martinelli, J. Phys. Chem. B, 2015, 119, 1611.
42 O. Hofft, S. Bahr, and V. Kempter, Langmuir, 2008, 24, 11562.
43 S. C. B. Myneni, S. J. Traina, G. A. Waychunas and T. J. Logan, Geochim. Cosmochim. Acta, 1998, 62, 3499.
44 B. Stuart. Infrared spectroscopy: Fundamentals and applications. J. Wiley & Sons, Ltd. Chichester, 2004.
45 R. Nadaf, M. Ijjada, J. Narayanan, B. Kutty, V. K. Aswal, J. R. Bellare and P. S. Goyal, AIP Conference Proceedings, 2013, 1512, 118.
46 J. Narayanan, A. S. Abdul Rasheed and J. R. Bellare, J. Colloid Interface Sci., 2008, 328, 67.
47 G. Colafemmina, D. Fiorentino, A. Ceglie, E. Carretti, E. Fratini, L. Dei, P. Baglioni, and G. Palazzo, J. Phys. Chem. B, 2007, 111, 7184.
48 T. Zemb and P. Charpin, Journal de Physique, 1985, 46, 249.
49 T. Singh, M. Drechsler, A.H.E. Mueeller, I. Mukhopadhyay and A. Kumar. Phys. Chem. Chem. Phys., 2010, 12, 1718.
50 A. Triolo, O. Russina, H.-J. Bleif and E. Di Cola, J. Phys. Chem. B, 2007, 111, 4641.
51 O. Russina, A. Triolo, L. Gontrani and R. Caminiti, J. Phys. Chem. Lett., 2012, 3, 27.
52 A. J. Carmichael, C. Hardacre, J. D. Holbrey, M. Nieuwenhuyzen and K. R. Seddon, Molecular Physics, 2001, 99, 795.
53 M. A. Firestone, P. G. Rickert, S. Seifert, S and M. L. Dietz, Inorg. Chim. Acta, 2004, 357, 3991.
54 A. E. Bradley, C. Hardacre, J. D. Holbrey, S. Johnston, S. E. J. McMath and M. Nieuwenhuyzen Chem. Mater., 2002, 14, 629.
55 F. Nilsson, O. Sodermann and I. Johansson, Langmuir, 1996, 12, 902.
56 I. Dierking, in Textures of Liquid Crystals, Wiley, Weinheim, 2003.
57 O. Green, S. Grubjesic, S. Lee and M. A. Firestone, J. Macromol. Sci. Part C: Polymer Reviews, 2009, 49, 339.
58 A.F. Kostko, B.H. Cipriano, O.A. Pinchuk, L. Ziserman, M.A. Anisimov, D. Danino and S.R. Raghavan. J. Phys. Chem. B, 2005, 109, 19126.
59 T. Méndez-Morales, J. Carrete, J. R. Rodríguez, O. Cabeza, L. J. Gallego, O. Russina and L. M. Varela, Phys. Chem. Chem. Phys., 2015, 17, 5298.
60 O. Russina, R. Caminiti, T. Méndez-Morales, J. Carrete, O. Cabeza, L. J. Gallego, L. M. Varela and A. Triolo, J. Mol. Liq., 2015, 205, 16.
61 T. Méndez-Morales, J. Carrete, O. Cabeza, O. Russina, A. Triolo, L. J. Gallego and L. M. Varela, J. Phys. Chem. B, 2014, 118, 761.
62 V. Gómez-González, B. Docampo-Álvarez, O. Cabeza, M. Fedorov, R. M. Lynden-Bell, L. J. Gallego and L. M. Varela, J. Chem. Phys., 2015, 143, 124507.
63 G. E. Walrafen, W.-H. Yang, Y. C. Chu and M. S. Hokmabadi, J. Solution Chem., 2000, 29, 905.
64 H. Shimura, M. Yoshio, K. Hoshino, T. Mukai, H. Ohno and T. Kato, J. Amer. Chem. Soc., 2008, 130, 1759.

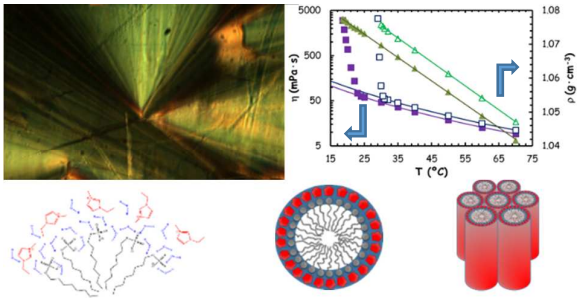

Mesomorphic liquid crystal character of aqueous EMIm-OSO_4 ionic liquid mixtures tuned with Mg sulfate salt addition. Effect on physical properties.